



PAPER

An initial study of complete 2D shear wave dispersion images using a reverberant shear wave field

RECEIVED
27 February 2019REVISED
4 June 2019ACCEPTED FOR PUBLICATION
6 June 2019PUBLISHED
16 July 2019Juvenal Ormachea¹, Kevin J Parker^{1,3} and Richard G Barr²¹ Department of Electrical and Computer Engineering, University of Rochester, Computer Studies Building, PO Box 270231, Rochester, NY 14627-0231, United States of America² Department of Radiology, Northeastern Ohio Medical University, Rootstown, Ohio and Southwoods Imaging, 7623 Market St., Youngstown, OH 44512, United States of America³ Author to whom any correspondence should be addressed.E-mail: kevin.parker@rochester.edu**Keywords:** reverberant shear wave field, shear dispersion, shear elastography, deep tissue viscoelasticity**Abstract**

Within the field of elastography, a relatively new approach analyzes the limiting case of shear waves established as a reverberant field. In this framework, it is assumed that a distribution of shear waves exists, oriented across all directions in 3D and continuous in time. The simultaneous multi-frequency application of reverberant shear wave fields can be accomplished by applying an array of external sources that can be excited by multiple frequencies within a bandwidth, for example 50, 100, 150, . . . , 500 Hz, all contributing to the shear wave field produced in the liver or other target organ. This enables the analysis of the dispersion of shear wave speed as it increases with frequency, indicating the viscoelastic and lossy nature of the tissue under study. Furthermore, dispersion images can be created and displayed alongside the shear wave speed images. We report preliminary studies on breast and liver tissues using the multi-frequency reverberant shear wave technique, employing frequencies up to 700 Hz in breast tissue, and robust reverberant patterns of shear waves across the entire liver and kidney in obese patients. Dispersion images are shown to have contrast between tissue types and with quantitative values that align with previous studies.

1. Introduction

Elastography is an imaging modality that estimates the biomechanical properties of tissues. Several groups have proposed different approaches to measure the shear wave speed (SWS), shear modulus, and other mechanical parameters to correlate them with the elastic tissue properties (Parker *et al* 2010, Barr 2014, Shiina *et al* 2015). However, it is known that soft tissues have viscoelastic properties and exhibit a frequency-dependent SWS, a phenomenon called dispersion. Generally, higher frequency shear wave components propagate faster than lower frequency components, and this dispersion can be measured over some bandwidth (Parker *et al* 2015).

The Radiological Society of North America Quantitative Imaging Biomarkers Alliance (RSNA/QIBA) (Palmeri *et al* 2015) attempted to obtain a better characterization of various calibrated phantoms across different imaging systems by measuring the SWS and linear dispersion at a reference frequency of 200 Hz. Urban *et al* (2017) measured the SWS dispersion over a wide range of frequencies (i.e. 60–600 Hz) in three different viscoelastic phantoms; the dispersion measurements helped to better differentiate the viscoelastic properties of these materials. Rouze *et al* (2018) also estimated the viscoelastic properties in calibrated phantoms by creating multiple lookup tables based on pair values of group SWS and dispersion at 200 Hz. In liver tissue, (Barry *et al* 2014, 2015) measured linear dispersion in 70 *ex vivo* lean and steatotic rat livers using crawling wave sonoelastography. These studies showed elevated linear dispersion in obese rats. Furthermore, an extended technical note reported by Parker *et al* (2015) summarized the importance of measuring dispersion in normal and steatotic livers in different studies using shear wave elastography (SWE). More recently, Hudert *et al* (2018) and Tzschatzsch *et al* (2015) measured the SWS and dispersion in *in vivo* liver tissue and correlated them with different grades of fibrosis using an external speaker that vibrates at multiple frequencies to generate shear waves. The vibration frequency (f_v) range was 30–60 Hz; however, it has been shown that dispersion is frequency dependent, and is

high at lower frequency ranges compared to higher frequencies (Parker *et al* 2018). In placenta tissue, Parker *et al* (2016) used the single tracking location acoustic radiation force technique to measure the SWS in *ex vivo* perfused samples and evaluated the SWS dispersion with a microchannel flow model. This study showed that dispersion increases after the administration of a vasoconstrictor agent compared with normal perfused placenta tissue. Furthermore, Callé *et al* (2018) and Simon *et al* (2018) analyzed the SWS dispersion using transient elastography and a rheological model in 20 and 10 *ex vivo* normal placenta tissues, respectively. Based on their results, dispersion may help to distinguish differences between placental structures. SWS dispersion was also related to the viscosity properties in kidney tissue. Amador *et al* (2011) applied shear wave dispersion ultrasound vibrometry (SDUV) over a bandwidth of 50–500 Hz in eight excised swine kidneys and found a statistical difference between shear elasticity and shear viscosity. Additionally, they measured an increase in dispersion of more than 30% after immersion in 10% formaldehyde. This study showed that the inhomogeneous structure of kidney can be better characterized by measuring both SWS and dispersion. SDUV has been used to estimate the viscoelastic properties in breast tissue over a frequency range of 50–400 Hz (Kumar *et al* 2018). Although SWS dispersion was not directly measured in this study, the viscoelastic properties of normal breast tissue and benign and malignant masses were obtained by fitting the SWS versus frequency curve with a Voigt model. Similarly, a previous study by Tanter *et al* (2008), measured the SWS in different breast lesions and showed a dispersion curve for the breast parenchyma over 100–400 Hz. This SWS frequency dependence curve illustrated why they were reporting higher SWS values compared to other studies that used lower mechanical frequencies and left open the question whether higher frequencies could provide better differentiation between benign and malignant breast lesions. As observed in these different studies, SWE may help to obtain a better characterization of the biomechanical and viscoelastic properties of tissues by additionally measuring the SWS dispersion.

Recently, Parker *et al* (2017) proposed and analyzed the limiting case of a fully reverberant shear wave elastography (R-SWE) field produced by sending continuous harmonic shear wave excitations to the tissue. Mathematically, this limiting case is modeled as the condition where shear waves of random amplitude and phase are found to be propagating in all directions across 4π steradians. Unlike other modalities, R-SWE does not filter or select for SWS propagation directions, which could make its implementation faster and simpler in an ultrasound system. This approach had been evaluated and compared with another well-known elastography technique in different calibrated phantoms (Ormachea *et al* 2018), *in vivo* liver and breast tissues using an ultrasound based method (Ormachea *et al* 2018), and in *ex vivo* pig cornea using an optical based method (Zveticovich *et al* 2018). These studies showed robust results across different tissue applications. In Ormachea *et al* (2018), the R-SWE approach was applied using individual and multi-vibration frequencies, obtaining similar SWS results for both types of experiments. Thus, the multi-frequency approach presents some advantages: it can more quickly assess the biomechanical tissue properties by estimating the SWS and dispersion, and the data is collected at the same time for different frequencies, which facilitates its use for clinical applications.

This study applied the multi-frequency R-SWE approach to quantify the viscoelastic properties of different media by evaluating the SWS and dispersion. Moreover, since this new modality obtains the SWS at different pixel locations over a broad vibration frequency range, a complete 2D image of dispersion is obtained and thus, an additional dispersion image can be created for better tissue characterization. In this work, two different calibrated CIRS phantoms, three *in vivo* livers, and two *in vivo* breast tissues were scanned as an initial study for 2D dispersion images using the R-SWE field.

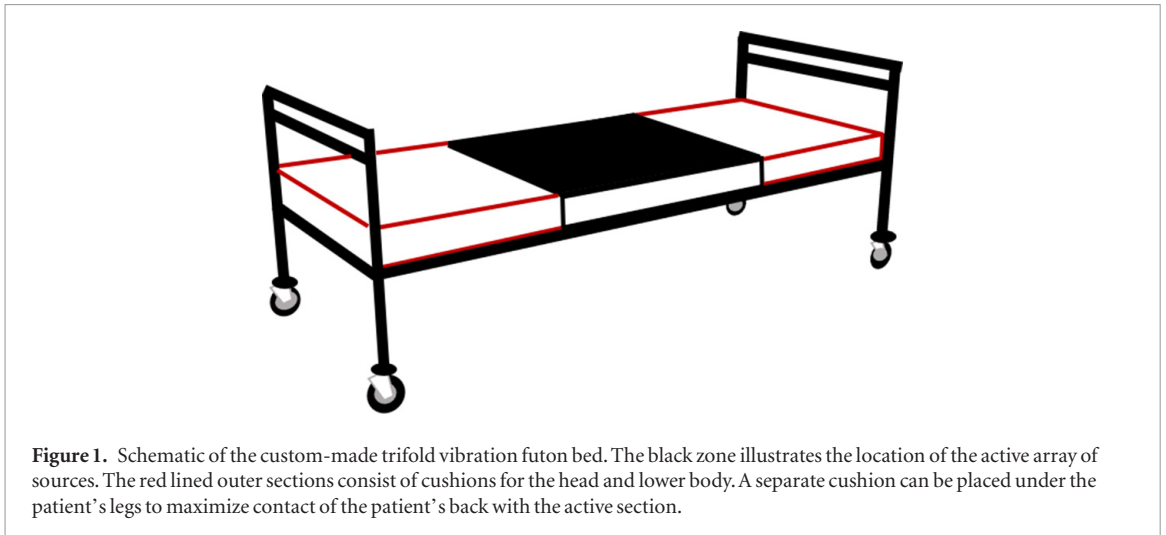
2. Methods

2.1. Ultrasound scanner and data acquisition

A Verasonics ultrasound system (Vantage-128TM, Verasonics, Kirkland, WA, USA), connected to a convex ultrasound probe (model C4-2, ATL, Bothell, WA, USA) or a linear ultrasound probe (model L7-4, ATL, Bothell, WA, USA) were used to track the induced displacements using a Loupas estimator (Loupas *et al* 1995). The linear probe was used for the breast phantom and breast tissue applications, whereas the convex probe was used for scan deeper in the viscoelastic phantom and liver tissue. A 3D matrix of in-phase and quadrature (IQ) data was stored for post-processing. The axial particle velocities are computed from frame-to-frame analysis of the acquired 3D IQ data. The center frequencies were 3 MHz and 5 MHz for the convex and linear probes, respectively. The sampling frequency were 12 MHz and 20 MHz for the convex and linear probes, respectively. The tracking pulse repetition frequency (PRF) was set to 3600 Hz with a total acquisition time of 0.5 s.

2.2. Vibration sources and multi-vibration frequency range

A custom-made portable trifold futon ($70 \times 60 \times 10 \text{ cm}^3$) with multiple embedded vibration sources (Quad Resonator Model EI718TM, Elastance Imaging LLC, Columbus, OH, USA) was mounted to a clinical bed to generate the reverberant shear wave field. The active vibration sources are located within the black region of figure 1 to couple displacements and shear waves into the body around the abdomen and liver. The active



area contains eight electromagnetic vibration drivers. Each one is 4 inches in diameter, and approximately 4Ω resistance with a neodymium core, and can be powered by standard audio amplifiers. Vibration frequency ranges between 50–500 Hz (steps of 50 Hz) and 40–400 Hz (steps of 40 Hz) were used for both CIRS phantoms and liver experiments. In addition, a frequency range of 117–702 Hz (steps of 117 Hz) was used for the breast experiments. All frequencies, from the selected vibration frequency range, were applied simultaneously in all the vibration sources for each experiment. The active surface was aligned with the rest of the futon surface to avoid discomfort in the patients. The precise details of the active source configuration are proprietary to Elastance Imaging LLC. Figure 1 shows a schematic of the custom-made trifold futon on top of the bed.

2.3. Noise reduction filtering

A filtering process similar to that used by Ormachea *et al* (2018) was applied. In this case each vibration frequency of the multi-frequency vibration range was processed using a low (f_{li}) and high (f_{hi}) cutoff frequencies of the finite impulse response (FIR) bandpass temporal filter. The cutoff frequencies were set at $f_{li} = (f_{vi} - 10)$ Hz and $f_{hi} = (f_{vi} + 10)$ Hz, where the subscript i indicates the corresponding i th frequency of the multi vibration frequency range. Additionally, the low (k_{li}) and high (k_{hi}) cutoff spatial frequencies (related to the wavenumber (k)) of the filter were set at $k_{li} = 2\pi f_{vi}/c_l$ and $k_{hi} = 2\pi f_{vi}/c_h$, where c_l and c_h are the minimum and maximum SWS limits and were set to 0.8 m s^{-1} , and 5 m s^{-1} for phantoms and liver experiments, respectively. For the breast experiments, c_l and c_h were set to 0.8 m s^{-1} , and 7 m s^{-1} , respectively.

2.4. Reverberant shear wave field and 2D SWS estimator

The wavenumber and, subsequently, the SWS were estimated using the method described by Parker *et al* (2017). The wavenumber was estimated by evaluating the second derivative of the autocorrelation function of the reverberant shear wave signal at the origin ($B_{vv}(0)$). This can be approximated by a finite difference. Thus:

$$|\hat{k}|^2 \cong C [\text{Re} \{B_{vv}(0)\} - \text{Re} \{B_{vv}(\Delta x)\}], \quad (1)$$

where C is a constant equal to $10/(\Delta x^2 B_{vv}(0))$, and the Δx lag and zero lag values of the real part of the autocorrelation at $\Delta t = 0$ from some segment of data are used. Further detailed analysis of the reverberant shear wave field and SWS estimation are found in Parker *et al* (2017).

The wavenumber and SWS can then be related using the equation:

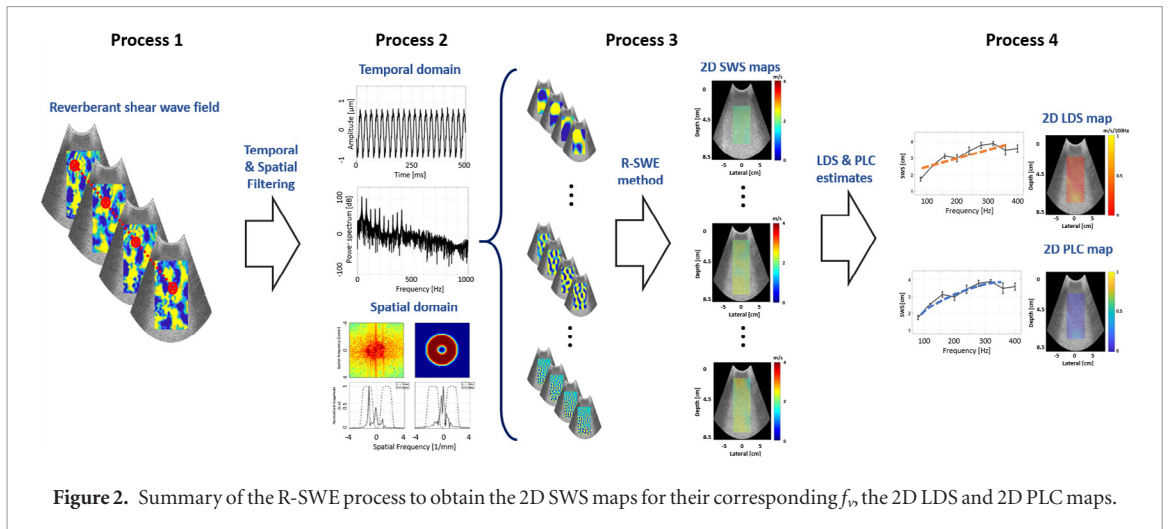
$$c_s(\omega) = \frac{2\pi f_v}{k} = \frac{\omega}{k} \quad (2)$$

where c_s is the SWS at a given vibration frequency and ω is the frequency in radians/s.

2.5. 2D linear dispersion slope and power law coefficient estimation

Shear wave phenomena are associated with harmonic and transient approaches. Harmonic schemes, including R-SWE, decompose a harmonic ensemble into their frequency components. When these techniques estimate shear wave propagation around a specific frequency, the results can be classified as phase velocity. In Parker *et al* (2018), it was shown that some viscoelastic phantoms and soft tissues exhibit a power law response. In these cases, the phase velocity can be written as:

$$c_s = c_1 \omega^a \quad (3)$$



where c_1 is the phase velocity measured at $\omega = 1 \text{ rad s}^{-1}$, and a is the power law coefficient.

In practice, the relationship between SWS and frequency is evaluated over the vibration frequency range. Frequently the simplest measurement of dispersion is the linear slope ($dc_s/d\omega$). However, this parameter has been found in tissues to vary strongly as a function of frequency. Considering a power law media, a simplification results if one plots c_s versus ω data on a log–log scale. In this case, the slope will be independent of frequency:

$$\frac{d(\log(c_s))}{d(\log(\omega))} = a. \quad (4)$$

In other words, the slope or dispersion as measured from a log–log plot of c_s versus ω will be constant across different frequency bands, whereas the slope from a linear plot will vary with frequency. Our multi-frequency data are analyzed for both the traditional linear (slope) dispersion and for power law dispersion by performing a linear regression fitting. This regression result is rejected if the goodness-of-fit metric $R^2 < 0.7$.

Figure 2 summarizes the process to obtain the 2D SWS maps for their corresponding f_v using the R-SWE approach, the final 2D linear dispersion slope (LDS), and the 2D power law coefficient (PLC) maps. ‘Process 1’ shows some snapshots from a movie of a typical R-SWE field using a multi-frequency range. Then, ‘Process 2’ illustrates the particle displacement in time and its corresponding frequency spectrum showing each f_v applied in the material. Additionally, it shows the spatial frequency spectrum from a 2D spatial domain matrix, the 2D spatial bandpass noise reduction filter, and two different profiles at the lateral and axial axes. After filtering each f_v , ‘Process 3’ applied the R-SWE method to obtain the 2D SWS maps. Finally, ‘Process 4’ takes the SWS and its corresponding frequency to measure the LDS and the PLC. The corresponding 2D image is obtained by repeating the process at each pixel location.

2.6. CIRS phantoms

The size and shape of the CIRS breast phantom (Model 059, Computerized Imaging Reference Systems, Norfolk, VA, USA) simulate a patient in the supine position; a homogeneous part (20 kPa nominal Young’s modulus) from the background region was chosen to evaluate R-SWE. Then, a custom made CIRS (Serial No. 2095.1-1, Computerized Imaging Reference Systems) homogeneous viscoelastic phantom (6 kPa nominal Young’s modulus) was chosen to evaluate R-SWE. The rectangular-shaped phantom was protected by a case with openings that allowed contact with the external vibration sources at two lateral borders.

2.7. *In vivo* liver and breast patients

Five healthy volunteer patients were scanned to evaluate the feasibility of applying the R-SWE modality in *in vivo* experiments. One thin and two obese patients were scanned for the *in vivo* liver experiments. Two patients, one with a breast fibroadenoma and one with dense breast tissue, were scanned for breast experiments. During the experiments, the patients reclined supine on the custom bed. These scans were conducted under the requirements of informed consent of the Southwoods Imaging Clinical Institutional Review Board.

3. Results

3.1. SWS in CIRS phantoms

Figure 3 shows the SWS, LDS, and PLC images superimposed on their corresponding B-mode image for the breast phantom. For LDS and PLC images, the frequency range of 200–500 Hz was selected because it meets

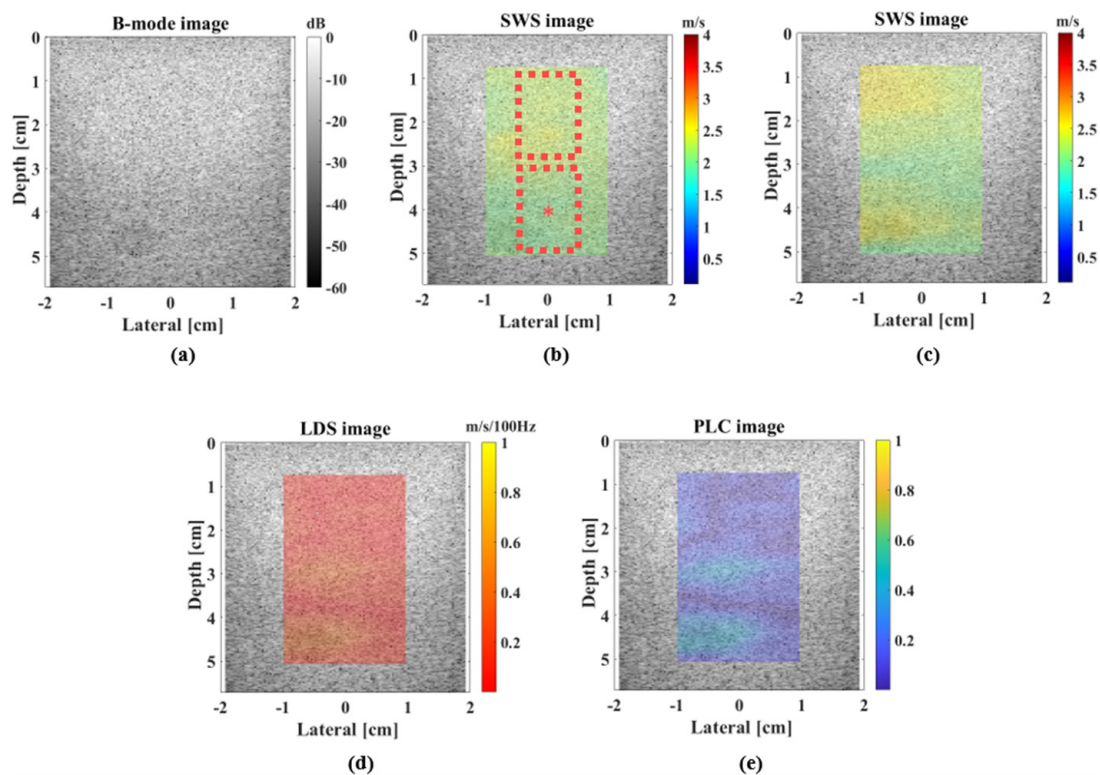


Figure 3. (a) B-mode images for the CIRS breast phantom, (b)–(c) SWS images, superimposed on their corresponding B-mode image, obtained with the R-SWE approach at two different vibration frequencies, 200 Hz and 300 Hz, respectively. (d) and (e) Linear dispersion slope and power law coefficient images using a 200–500 Hz frequency range. The dashed-line rectangles illustrate the selected ROIs (only shown in one image for reference purposes) to calculate mean and standard deviation values showed in table 1. The ‘*’ symbol illustrates the center point of one ROI that was used to plot dispersion curves in figure 5(a).

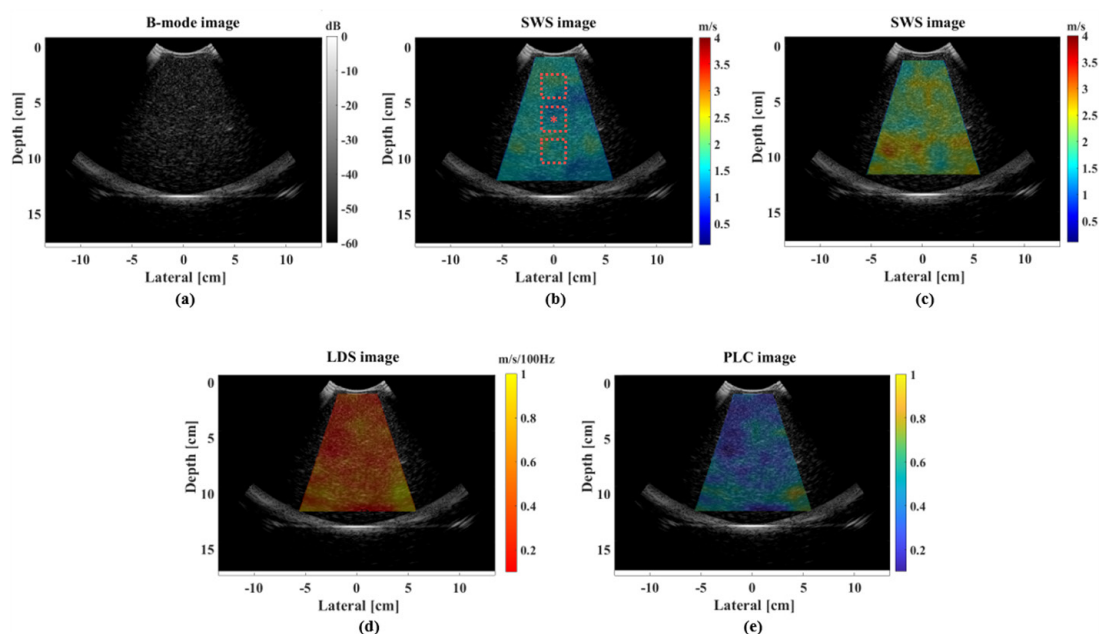


Figure 4. (a) B-mode images for the CIRS viscoelastic phantom, (b)–(c) SWS images, superimposed on their corresponding B-mode image, obtained with the R-SWE approach at two different vibration frequencies, 80 Hz and 200 Hz, respectively. (d) and (e) Linear dispersion slope and power law coefficient images using a 80–320 Hz frequency range. The dashed-line squares illustrate the selected ROIs (only shown in one image for reference purposes) to calculate mean and standard deviation values showed in table 1. The ‘*’ symbol illustrates the center point of one ROI that was used to plot dispersion curves in figure 5(b).

the established fitting rule ($R^2 > 0.7$). Subsequently, two regions of interest (ROI) of $2 \times 1 \text{ cm}^2$ were extracted at 1.8 cm and 4 cm depth for each image to obtain a reference mean SWS, LDS, and PLC and their standard deviations (SD). Figure 4 shows the SWS, LDS, and PLC maps superimposed on their corresponding B-mode

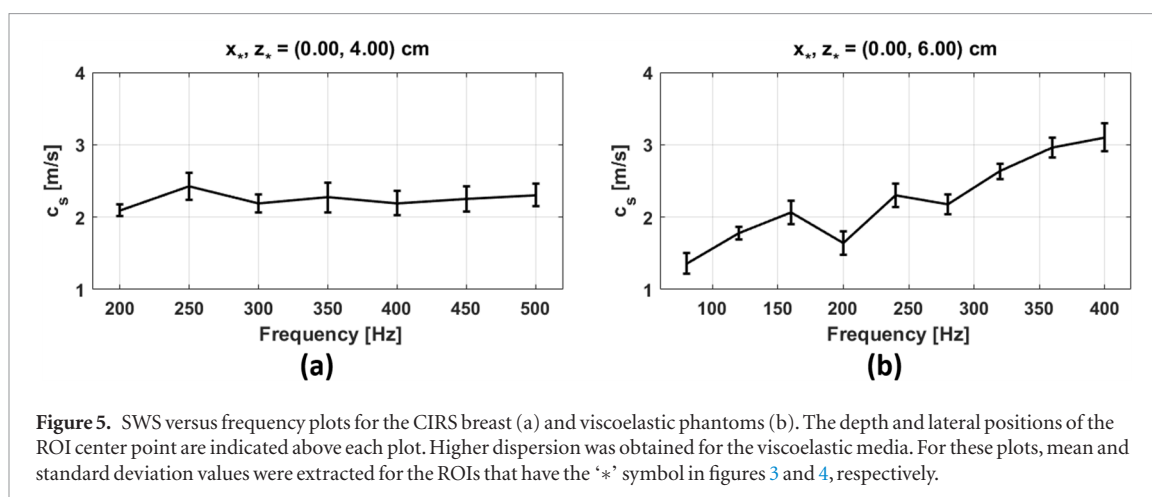


Figure 5. SWS versus frequency plots for the CIRS breast (a) and viscoelastic phantoms (b). The depth and lateral positions of the ROI center point are indicated above each plot. Higher dispersion was obtained for the viscoelastic media. For these plots, mean and standard deviation values were extracted for the ROIs that have the ‘*’ symbol in figures 3 and 4, respectively.

Table 1. Summary of viscoelastic material properties in different media.

Media	f_v [Hz]	SWS [m s^{-1}]	LDS [$\text{m s}^{-1}/100 \text{ Hz}$]	PLC	f_v range [Hz]	R^2 for LDS	R^2 for PLC
Breast phantom	200	2.15 ± 0.11	0.10 ± 0.02	0.18 ± 0.11	200–500	0.77 ± 0.14	0.73 ± 0.12
Viscoelastic phantom	200	1.88 ± 0.38	0.42 ± 0.02	0.34 ± 0.03	80–320	0.73 ± 0.05	0.71 ± 0.07
Patient #1, liver thin case	200	1.99 ± 0.19	0.28 ± 0.14	0.23 ± 0.10	80–320	0.92 ± 0.05	0.90 ± 0.07
Patient #2, liver obese case	200	2.29 ± 0.37	0.49 ± 0.17	0.44 ± 0.09	80–320	0.82 ± 0.14	0.80 ± 0.12
Patient #3, liver obese case	200	2.38 ± 0.20	0.54 ± 0.19	0.43 ± 0.04	80–320	0.75 ± 0.14	0.72 ± 0.17
Patient #4, breast fibroadenoma case	702	3.71 ± 0.29	0.29 ± 0.04	0.54 ± 0.32	468–702	0.72 ± 0.09	0.75 ± 0.11
Patient #5, dense breast tissue case	702	4.33 ± 0.34	0.48 ± 0.15	0.58 ± 0.21	468–702	0.96 ± 0.12	0.95 ± 0.17

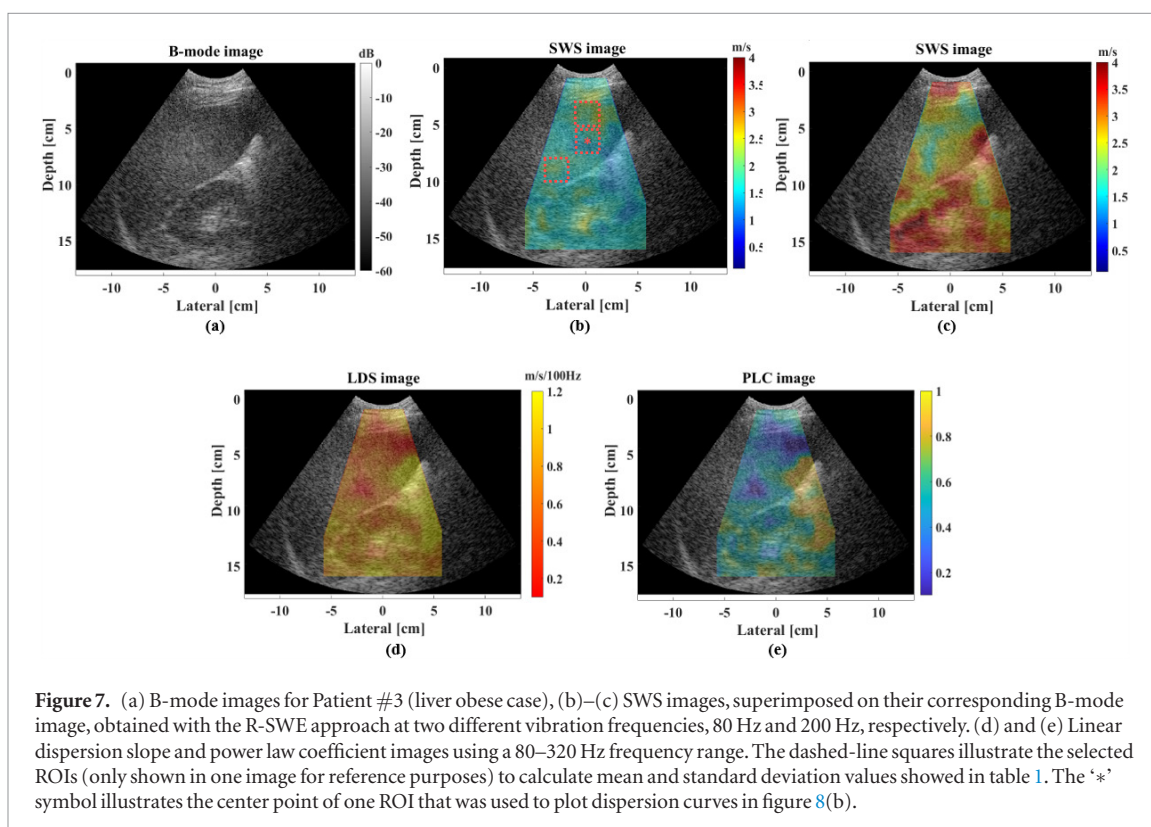
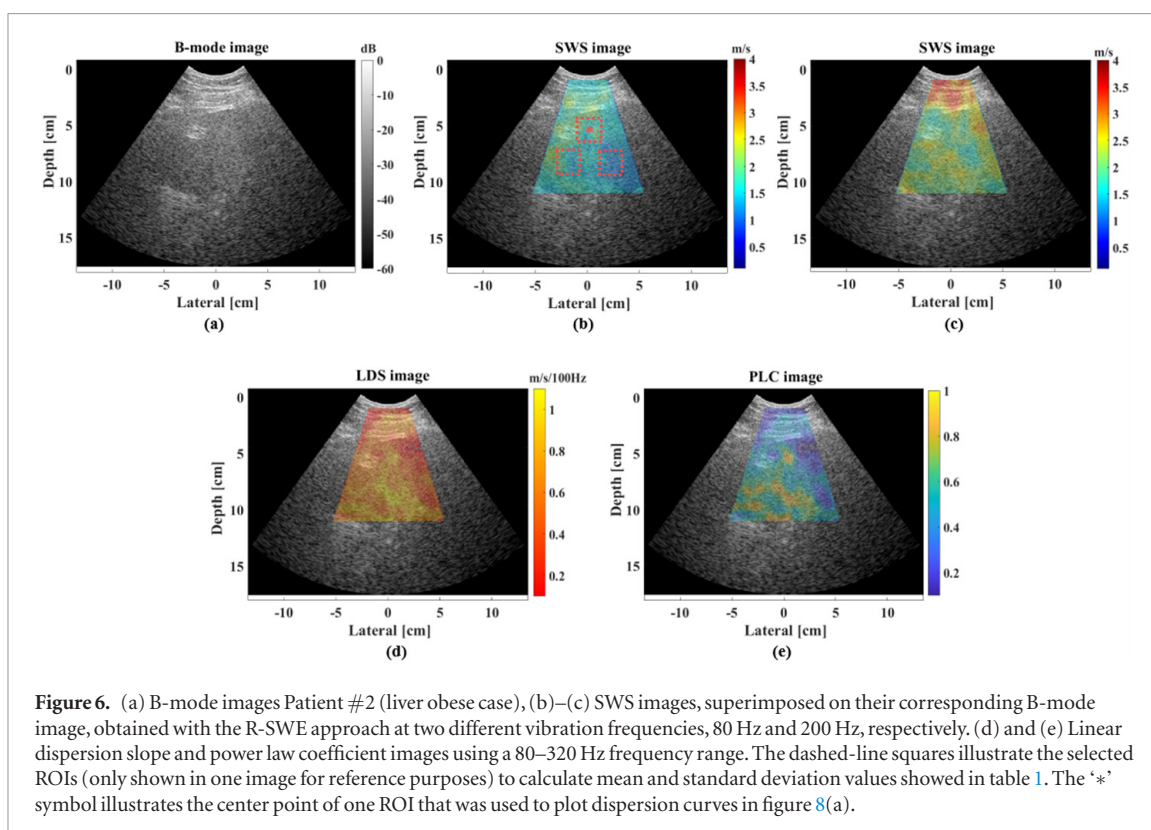
image for the viscoelastic phantom. For LDS and PLC images, the frequency range of 80–320 Hz was selected because it meets the established fitting rule ($R^2 > 0.7$). For this case, three ROIs of $2 \times 2 \text{ cm}^2$ size were selected at different positions, since the convex probe covers a bigger field of view, to obtain reference mean SWS, LDS, and PLC and their SD, at 4 cm, 6 cm, and 8 cm depth. Figure 5 shows a reference plot of SWS as a function of frequency, extracted from the ROIs with the ‘*’ symbol at the center region, for both phantoms. As expected, the SWS remained nearly constant for the breast phantom since it is a nearly elastic material (LDS = $0.10 \pm 0.02 \text{ m s}^{-1}/100 \text{ Hz}$; PLC = 0.18 ± 0.11). On the other hand, the SWS increased with an increasing frequency for the viscoelastic phantom (LDS = $0.42 \pm 0.02 \text{ m s}^{-1}/100 \text{ Hz}$; PLC = 0.34 ± 0.03). Additionally, the goodness of the fit curve, represented by the R^2 value, is also reported for each LDS and PLC result in table 1.

3.2. *In vivo* liver elastography results

For the *in vivo* liver experiments, three ROIs of $2 \times 2 \text{ cm}^2$ size were located at different positions to obtain a reference mean SWS, LDS, and PLC and their SD. Figures 6 and 7 show the different viscoelastic images for the obese patients. For LDS and PLC images, the frequency range of 80–320 Hz was selected because it is a similar and comparable frequency range to the various liver studies that measured the linear dispersion (Parker *et al* 2015), and the range met the established fitting rule ($R^2 > 0.7$). A distinction between fat/muscle and liver tissue were obtained for frequencies higher than 100 Hz for all cases. The liver is located between 4–11 cm depth and 4–10 cm depth in figures 6 and 7, respectively. Thus, R-SWE was able to measure the viscoelastic properties of liver tissue in obese patients at deep regions. Additionally, it can be observed that the kidney was also measured in figure 7. For this case, a simple observation at 200 Hz shows a clearer distinction between the kidney cortex and the liver tissue. Although this suggests that R-SWE may be able to measure the viscoelastic properties in kidney tissue, further research is needed with more focus in this organ. Figure 8 shows a reference plot of SWS as a function of frequency, extracted from the ROIs with the ‘*’ symbol at the center region, for both obese liver patients. Both patients show higher LDS and PLC results than the thin patient’s liver and (see table 1 for details). Additionally, the goodness of the fit curve, represented by the R^2 value, is also reported for each LDS and PLC results in table 1.

3.3. *In vivo* breast elastography results

Figure 9 shows the breast experiment with the benign fibroadenoma. The SWS maps illustrate the presence of the lesion that has a lower SWS than the surrounding tissue. Three ROIs of $0.5 \times 0.5 \text{ cm}^2$ were selected to cover



the fibroadenoma lesion to obtain the mean SWS, LDS, and PLC reference values. The SWS value was lower than benign masses reported in Barr *et al* (2015). Figure 10 shows the viscoelastic results for the dense breast tissue experiment, a ROI of $1 \times 2 \text{ cm}^2$ was selected to cover the dense breast tissue area, the mean SWS of $4.33 \pm 0.34 \text{ m s}^{-1}$ and $3.77 \pm 0.09 \text{ m s}^{-1}$ for the dense and fat regions were obtained, respectively. Figure 11 shows a reference plot of SWS as a function of frequency, extracted from the ROIs with the ‘*’ symbol at the center region, for both breast cases. For LDS and PLC images, the frequency range of 468–702 Hz was selected because SWS images showed better contrast difference between the fibroadenoma lesion/surrounding tissue, and fat/dense-breast-tissue regions at this vibration frequency range. Further, the established fitting rule ($R^2 > 0.7$) was met.

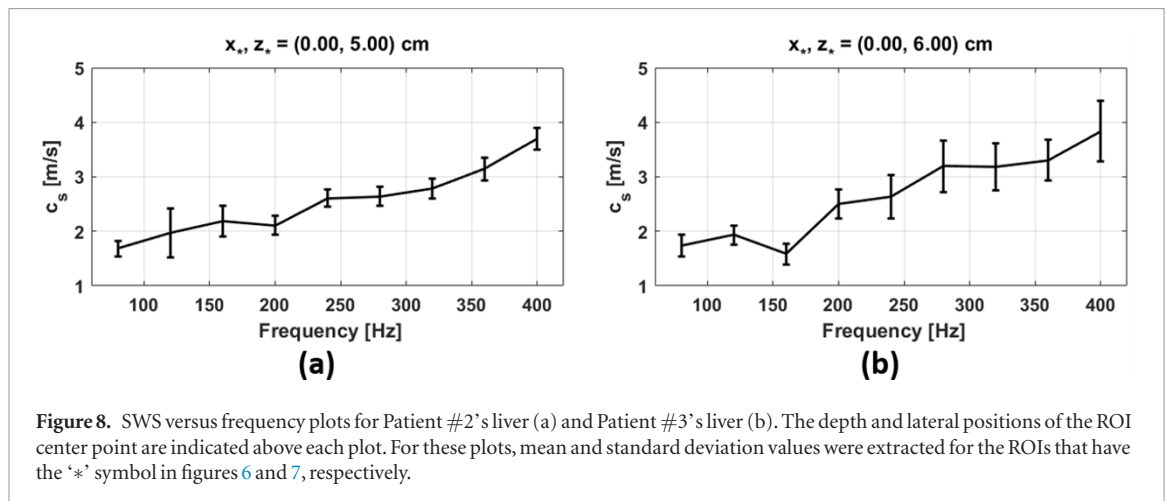


Figure 8. SWS versus frequency plots for Patient #2's liver (a) and Patient #3's liver (b). The depth and lateral positions of the ROI center point are indicated above each plot. For these plots, mean and standard deviation values were extracted for the ROIs that have the '*' symbol in figures 6 and 7, respectively.

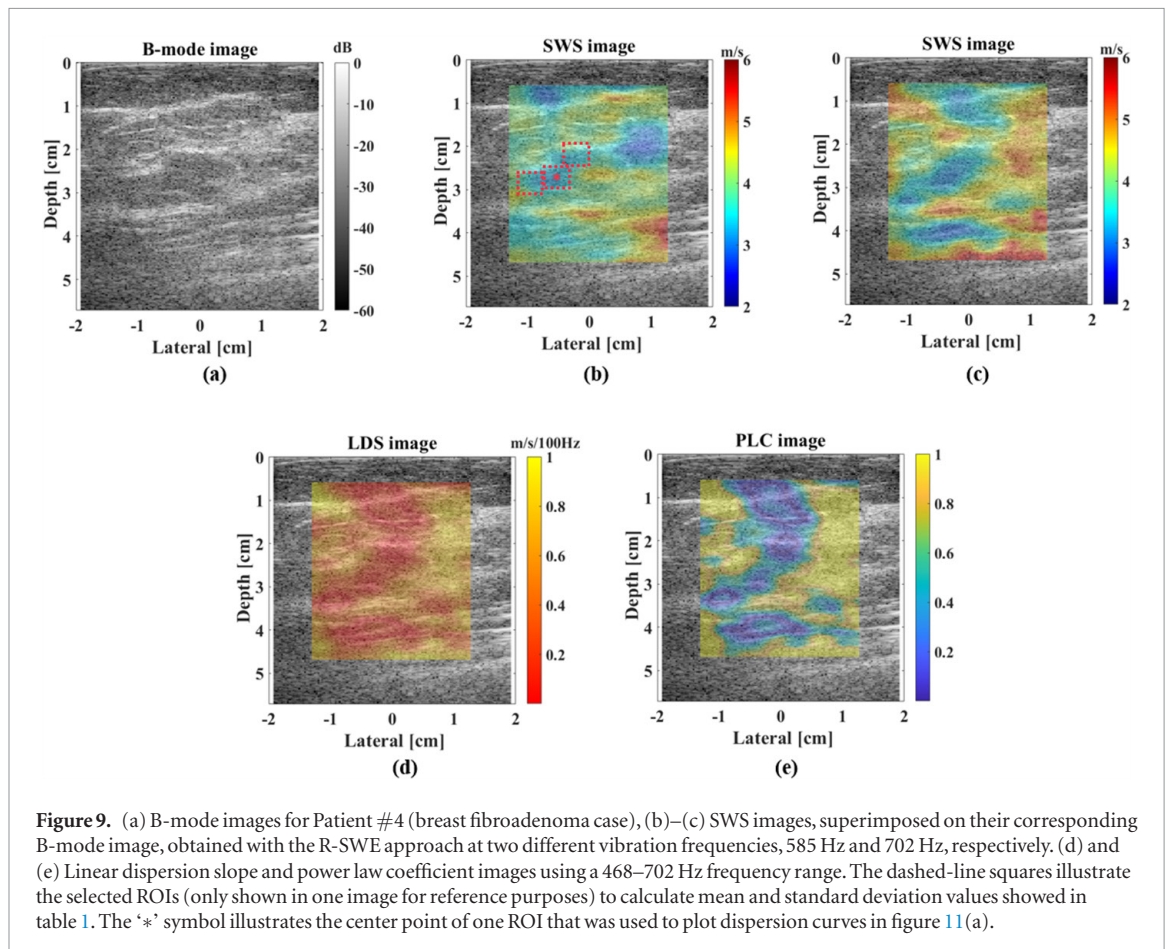
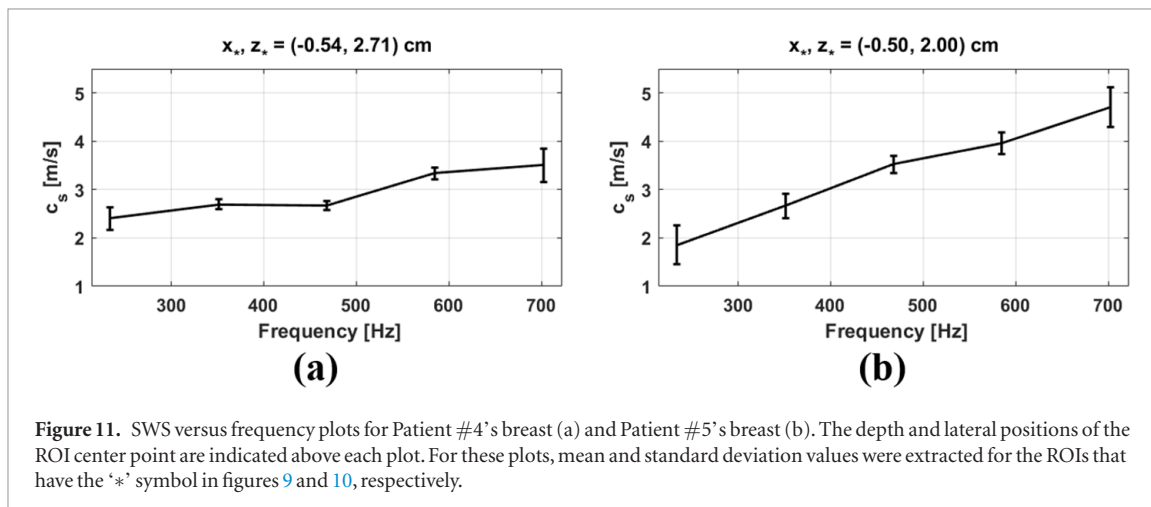
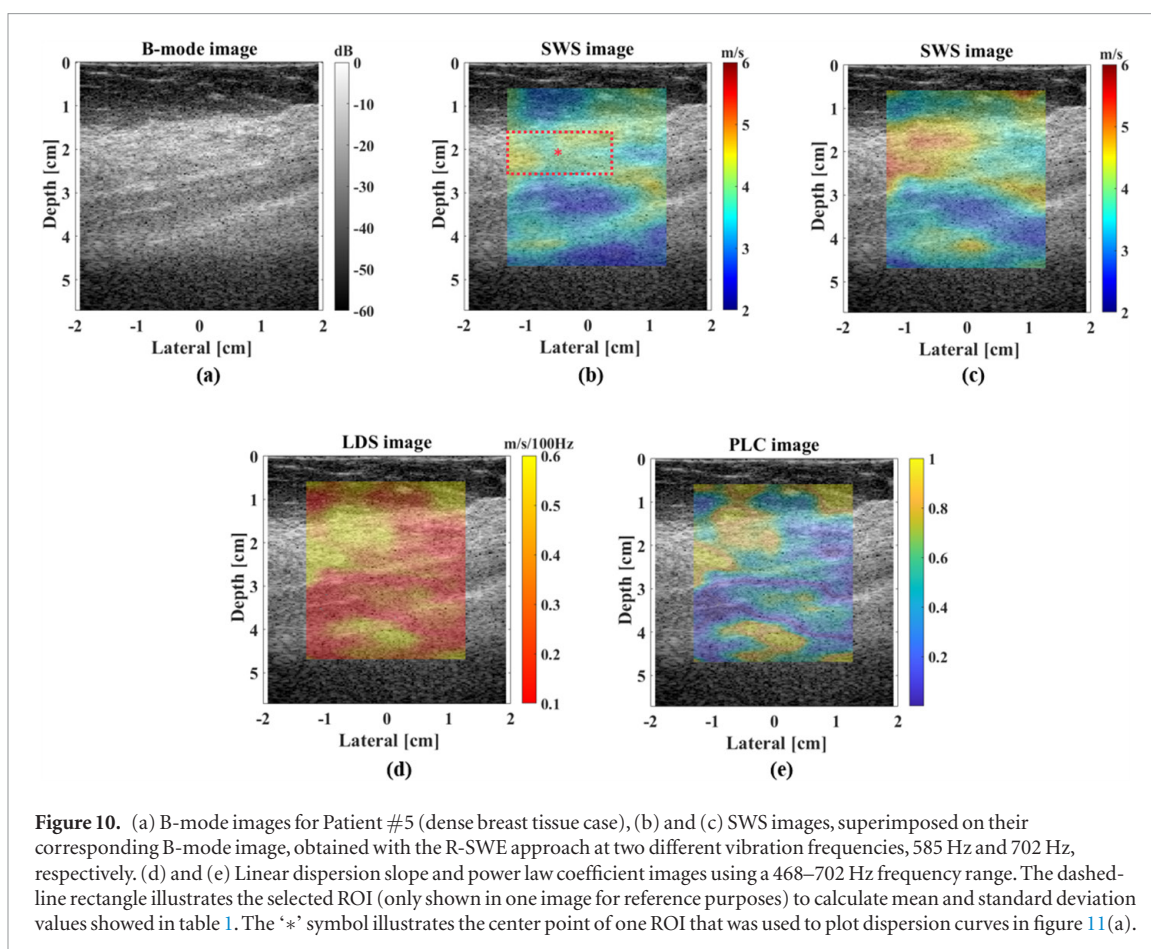


Figure 9. (a) B-mode images for Patient #4 (breast fibroadenoma case), (b)–(c) SWS images, superimposed on their corresponding B-mode image, obtained with the R-SWE approach at two different vibration frequencies, 585 Hz and 702 Hz, respectively. (d) and (e) Linear dispersion slope and power law coefficient images using a 468–702 Hz frequency range. The dashed-line squares illustrate the selected ROIs (only shown in one image for reference purposes) to calculate mean and standard deviation values showed in table 1. The '*' symbol illustrates the center point of one ROI that was used to plot dispersion curves in figure 11(a).

Additionally, the goodness of the fit curve, represented by the R^2 value, is also reported for each LDS and PLC result in table 1.

4. Discussion

A multi-frequency 3D reverberant shear wave field was created in different media, and quantitative estimates of SWS and dispersion were calculated within the entire field of view of B-scan image planes. For all of these, SWS and dispersion maps were obtained using the R-SWE approach. The new dispersion images enabled better characterization of the viscoelastic properties of different tissues in a complete 2D field of view. The results in the CIRS phantoms illustrated the capability of R-SWE to differentiate between elastic and viscoelastic media by measuring the SWS frequency dependence. Additionally, the homogeneity in the SWS and LDS maps is consistent with the homogeneous composition for each material. It is shown that the dispersion is lower for the almost purely elastic breast phantom (i.e. 0.10 ± 0.02 m s⁻¹/100 Hz) than the viscoelastic phantom (i.e. 0.42 ± 0.02 m s⁻¹/100 Hz).



For the *in vivo* liver scans, the R-SWE approach was applied in one thin and two obese patients. It is worth mentioning that this technique was able to measure the viscoelastic properties at deep areas (~ 16 cm depth) in obese patients. As can be seen in figures 6 and 7, a clear difference between the fat/muscle layer and liver tissue was obtained at vibration frequencies higher than 100 Hz. To the best of the authors' knowledge, this is the first study that attempted to measure the liver viscoelastic properties in obese patients using vibration frequencies up to 400 Hz at deep areas. Thus, the R-SWE approach may be able to overcome one of the main clinical limitations of applying elastography to the liver: the ability to obtain a SWS image in obese cases (Ferraioli *et al* 2015) throughout the liver volume. For each patient, the mean SWS obtained at 200 Hz is presented in table 1. The reported SWS is lower than 2.5 m s^{-1} ; this value is mentioned because it illustrates a threshold to differentiate low fibrosis ($< \text{F2}$) from high Fibrosis ($> \text{F3}$) at 200 Hz in Nightingale *et al* (2015). In that sense, our results are reasonable since none of the scanned patients have a confirmed high score. Additionally, a low LDS value was obtained for the thin liver patient compared to the two obese patients (see table 1). Linear dispersion values were approximately between 0.1 and $0.6 \text{ m s}^{-1}/100 \text{ Hz}$ using a frequency range of 0–400 Hz in

Nightingale *et al* (2015). Furthermore, (Deffieux *et al* 2009, Muller *et al* 2009) found a LDS value equal to $0.36 \pm 0.06 \text{ m s}^{-1}/100 \text{ Hz}$ in *in vivo* healthy human volunteers using frequencies ranges of 40–450 Hz and 60–390 Hz, respectively, which is slightly higher than the LDS value we obtained in our thin liver patient. The results obtained in our studies and comparisons of these results with other liver studies illustrates that the R-SWE approach can measure the viscoelastic properties in *in vivo* liver tissue, in obese patients and at deep areas. Further research is needed to evaluate this modality in patients at different stages of fibrosis or steatosis.

For the *in vivo* breast scans, a patient with a fibroadenoma and a patient with a dense breast tissue were imaged. In both cases, higher vibration frequencies, up to 702 Hz, were applied because breast tissue stiffness is usually higher than liver tissue (Barr *et al* 2015, Ferraioli *et al* 2015) and shorter shear wavelengths could be obtained to improve the spatial resolution of the R-SWE approach to detect lesions. For the fibroadenoma patient, a mean SWS of $3.71 \pm 0.29 \text{ m s}^{-1}$ was obtained at 702 Hz inside the lesion. Following the ‘aggressive rule’ proposed by Barr *et al* (2015), the lesion could be considered as a ‘low stiffness lesion’. Similarly, according to Elseedawy *et al* (2016), this breast mass could be considered as a soft fibroadenoma because it meets the following characteristics: the lesion stiffness ($<4.08 \text{ m s}^{-1}$), the patient’s age (<50 years), and the lesion diameter size ($<1.5 \text{ cm}$). In our second breast experiment, the dense breast tissue case, a mean SWS of $4.33 \pm 0.34 \text{ m s}^{-1}$ was obtained within the dense tissue area at 702 Hz. This SWS value indicates that it is a benign mass because it is lower than 5.2 m s^{-1} (Chang *et al* 2011, Barr *et al* 2015). Another parameter we can include to classify this mass as a benign lesion is the mass/fat ratio proposed by Çebi Olgun *et al* (2014). In this study, the mass/fat ratio was measured in 115 patients with different breast lesions and it was found that a ratio lower than 4.6 helps to differentiate benign and malignant breast lesions. In our results, the dense tissue /fat ratio was equal to 1.32 (56.25 kPa/42.64 kPa) using the mean SWS values of 4.33 m s^{-1} and 3.77 m s^{-1} for the dense breast tissue and fat regions, respectively. An analysis of the LDS results for breast tissue and what these numbers could mean diagnostically is currently unknown due to the lack of dispersion studies in breast using SWE. Kumar *et al* (2018) analyzed the phase SWS with respect to frequency in normal, benign, and malignant breast tissues in 43 patients. They found significant differences between the shear viscosity of benign and malignant lesions: higher shear viscosity values were reported for malignant lesions than benign lesions. One hypothesis therefore is that benign lesions should have lower dispersion values. In our study, LDS for the fibroadenoma case was less than that for the dense breast tissue, but both cases were within the range of the LDS values for our liver patients, and furthermore, both breast cases represent benign lesions. Future studies are needed to determine ‘low’ and ‘high’ thresholds for dispersion in breast tissue, as well as other clinically relevant factors such as (a) the frequency range to measure the LDS (in this preliminary study it was higher than that used for the liver cases), (b) the surrounding tissue properties (fat, dense, mixed), and (c) age effects. What is encouraging is that the LDS images show additional contrast between the fibroadenoma lesion and surrounding tissue as well as between the dense breast tissue and the fat region. Further studies applying the R-SWE approach are planned to obtain a better characterization of breast lesions using both SWS and LDS images.

The other parameter we reported was the PLC. The results for the CIRS phantoms show a clear difference between the almost purely elastic (0.18 ± 0.11) and the viscoelastic (0.34 ± 0.03) phantoms. In Parker *et al* (2018), a PLC equal to 0.48 was obtained for the same viscoelastic phantom but using a discrete frequency range of 80–220 Hz. The mean PLC results for the *in vivo* livers also show a difference between the thin liver (0.25 ± 0.04) and the obese liver cases (Patient#2: 0.44 ± 0.09 ; Patient#3: 0.43 ± 0.04) indicating that the PLC may be an additional parameter that could help to differentiate the tissue viscoelastic properties. Other studies also measured the PLC in *in vivo* healthy livers. Parker *et al* (2018) reported a PLC equal to 0.47 from discrete frequencies of 100–240 Hz and Zhang and Holm (2016) showed a table summarizing different PLC values reported in the literature: the reported PLC values were 0.18 from 25–62.5 Hz using magnetic resonance elastography (MRE) and 0.5 from 75 to 600 Hz using shear wave spectroscopy. For our *in vivo* breast results, the mean PLC values also differ from the fibroadenoma (0.54 ± 0.32) and the dense breast tissue (0.58 ± 0.21). Zhang and Holm (2016) reported a PLC of 0.85 for malignant breast tumors using MRE. On the other hand, Sinkus *et al* (2007) obtained a PLC of 0.84 for a healthy breast volunteer using MRE. Both MRE studies used similar frequency ranges, 60–100 Hz and 65–100 Hz, respectively. However, in order to compare the PLC values from our study with those from Sinkus *et al* (2007) and Zhang and Holm (2016), we needed to divide their reported PLC by a factor of 2, since they reported the shear modulus power law while we report the SWS power law. The theories that interrelate these different approaches can be found in Parker *et al* (2018).

As it can be observed, in cases where a power law model has been explicitly applied, estimates of the power law parameter are wide-ranging and thus further studies are needed to determine what PLC can add to clinical differentiation of tissues based on better characterization of their viscoelastic properties.

Finally, a practical issue for clinicians concerns the time required for data acquisition and processing of the estimator images, particularly for ultrasound systems that are intended for real time operation. Currently, the SWS and dispersion results are obtained via post processing and are not implemented as a real time operation. However, high frame rate ultrasound scanning and high complexity shear wave algorithms are already imple-

mented on a number of ultrasound systems, so the limiting factor may be the time required to acquire a satisfactory estimate of the reverberant autocorrelation function. For this study, the total acquisition time was 0.5 s to track at least 10 periods for the lower frequency component of the multi-frequency vibration range. Of course, less time may be necessary depending on noise and unwanted tissue motion, however this illustration points to the possibility of reverberant elastography frame rates that are perceived as real time.

5. Conclusion

This proof of concept study demonstrates that reverberant shear wave fields can be produced in deep tissues from external sources, up to 400 Hz in obese patients' livers and over 700 Hz in breast tissue. The use of multi-frequency tones simultaneously applied enables a rapid collection of shear wave response and then the analysis of SWS and dispersion at discrete frequencies. The dispersion can be analyzed as a slope (change in SWS with change in frequency), or as a power law coefficient consistent with a more advanced framework of tissue rheology. These dispersion estimates are then obtained over the entire ROI and used to form dispersion images. These may provide additional information and image contrast in cases where lesions or pathologies demonstrate an altered viscoelastic response, and therefore an altered dispersion parameter, compared with normal tissue. Further study is required to define the practical upper limits to shear wave frequencies applied to the breast or liver within our framework, and the range of normal dispersions expected within a healthy population.

Acknowledgments

Juvenal Ormachea was supported by Peruvian Government scholarship 213-2014-FONDECYT. This work was supported by the Hajim School of Engineering and Applied Sciences at the University of Rochester. We are grateful to Elastance Imaging for the loan of their Quad Resonator.

ORCID iDs

Juvenal Ormachea  <https://orcid.org/0000-0003-2481-8133>

Kevin J Parker  <https://orcid.org/0000-0002-6313-6605>

References

- Amador C, Urban M W, Chen S and Greenleaf J F 2011 Shearwave dispersion ultrasound vibrometry (SDUV) on swine kidney *IEEE Trans. Ultrason. Ferroelectr. Freq. Control* **58** 2608–19
- Barr R G 2014 Elastography in clinical practice *Radiol. Clin. North Am.* **52** 1145–62
- Barry C T, Hah Z, Partin A, Mooney R A, Chuang K H, Augustine A, Almudevar A, Cao W, Rubens D J and Parker K J 2014 Mouse liver dispersion for the diagnosis of early-stage fatty liver disease: a 70-sample study *Ultrasound Med. Biol.* **40** 704–13
- Barry C T, Hazard C, Hah Z, Cheng G, Partin A, Mooney R A, Chuang K H, Cao W, Rubens D J and Parker K J 2015 Shear wave dispersion in lean versus steatotic rat livers *J. Ultrasound Med.* **34** 1123–9
- Barr R G et al 2015 WFUMB guidelines and recommendations for clinical use of ultrasound elastography: part 2: breast *Ultrasound Med. Biol.* **41** 1148–60
- Callé S, Simon E, Dumoux M-C, Perrotin F and Remenieras J-P 2018 Shear wave velocity dispersion analysis in placenta using 2D transient elastography *J. Appl. Phys.* **123** 234902
- Çebi Olgun D, Korkmazer B, Kılıç F, Dikici A S, Velidedeoğlu M, Aydoğan F, Kantarcı F and Yılmaz M H 2014 Use of shear wave elastography to differentiate benign and malignant breast lesions *Diagn. Interv. Radiol.* **20** 239–44
- Chang J M, Moon W K, Cho N, Yi A, Koo H R, Han W, Noh D Y, Moon H G and Kim S J 2011 Clinical application of shear wave elastography (SWE) in the diagnosis of benign and malignant breast diseases *Breast Cancer Res. Treat.* **129** 89–97
- Deffieux T, Montaldo G, Tanter M and Fink M 2009 Shear wave spectroscopy for *in vivo* quantification of human soft tissues visco-elasticity *IEEE Trans. Med. Imaging* **28** 313–22
- Elseedawy M, Whelehan P, Vinnicombe S, Thomson K and Evans A 2016 Factors influencing the stiffness of fibroadenomas at shear wave elastography *Clin. Radiol.* **71** 92–5
- Ferraioli G et al 2015 WFUMB guidelines and recommendations for clinical use of ultrasound elastography: part 3: liver *Ultrasound Med. Biol.* **41** 1161–79
- Hudert C A et al 2018 US time-harmonic elastography: detection of liver fibrosis in adolescents with extreme obesity with nonalcoholic fatty liver disease *Radiology* **288** 99–106
- Kumar V, Denis M, Gregory A, Bayat M, Mehrmohammadi M, Fazzio R, Fatemi M and Alizad A 2018 Viscoelastic parameters as discriminators of breast masses: initial human study results *PLoS One* **13** e0205717
- Loupas T, Powers J T and Gill R W 1995 An axial velocity estimator for ultrasound blood flow imaging, based on a full evaluation of the Doppler equation by means of a two-dimensional autocorrelation approach *IEEE Trans. Ultrason. Ferroelectr. Freq. Control* **42** 672–88
- Muller M, Gennisson J L, Deffieux T, Tanter M and Fink M 2009 Quantitative viscoelasticity mapping of human liver using supersonic shear imaging: preliminary *in vivo* feasibility study *Ultrasound Med. Biol.* **35** 219–29
- Nightingale K R, Rouze N C, Rosenzweig S J, Wang M H, Abdelmalek M F, Guy C D and Palmeri M L 2015 Derivation and analysis of viscoelastic properties in human liver: impact of frequency on fibrosis and steatosis staging *IEEE Trans. Ultrason. Ferroelectr. Freq. Control* **62** 165–75

- Ormachea J, Castaneda B and Parker K J 2018 Shear wave speed estimation using reverberant shear wave fields: implementation and feasibility studies *Ultrasound Med. Biol.* **44** 963–77
- Palmeri M et al 2015 *IEEE Int. Ultrasonics Symp.* (21–24 October 2015) pp 1–4
- Parker K J, Doyley M M and Rubens D J 2010 Imaging the elastic properties of tissue: the 20 year perspective *Phys. Med. Biol.* **56** R1–29
- Parker K J, Ormachea J and Hah Z 2018 Group versus phase velocity of shear waves in soft tissues *Ultrason. Imaging* **40** 343–56
- Parker K J, Ormachea J, McAleavy S A, Wood R W, Carroll-Nellenback J J and Miller R K 2016 Shear wave dispersion behaviors of soft, vascularized tissues from the microchannel flow model *Phys. Med. Biol.* **61** 4890–903
- Parker K J, Ormachea J, Zvietcovich F and Castaneda B 2017 Reverberant shear wave fields and estimation of tissue properties *Phys. Med. Biol.* **62** 1046–61
- Parker K J, Partin A and Rubens D J 2015 What do we know about shear wave dispersion in normal and steatotic livers? *Ultrasound Med. Biol.* **41** 1481–7
- Rouze N C, Deng Y, Trutna C A, Palmeri M L and Nightingale K R 2018 Characterization of viscoelastic materials using group shear wave speeds *IEEE Trans. Ultrason. Ferroelectr. Freq. Control* **65** 780–94
- Shiina T et al 2015 WFUMB guidelines and recommendations for clinical use of ultrasound elastography: part 1: basic principles and terminology *Ultrasound Med. Biol.* **41** 1126–47
- Simon E G, Calle S, Perrotin F and Remenieras J P 2018 Measurement of shear wave speed dispersion in the placenta by transient elastography: a preliminary *ex vivo* study *PLoS One* **13** e0194309
- Sinkus R, Siegmann K, Xydeas T, Tanter M, Claussen C and Fink M 2007 MR elastography of breast lesions: understanding the solid/liquid duality can improve the specificity of contrast-enhanced MR mammography *Magn. Reson. Med.* **58** 1135–44
- Tanter M, Bercoff J, Athanasiou A, Deffieux T, Gennisson J L, Montaldo G, Muller M, Tardivon A and Fink M 2008 Quantitative assessment of breast lesion viscoelasticity: initial clinical results using supersonic shear imaging *Ultrasound Med. Biol.* **34** 1373–86
- Tzschatzsch H, Ipek-Ugay S, Trong M N, Guo J, Eggers J, Gentz E, Fischer T, Schultz M, Braun J and Sack I 2015 Multifrequency time-harmonic elastography for the measurement of liver viscoelasticity in large tissue windows *Ultrasound Med. Biol.* **41** 724–33
- Urban M W, Chen J and Ehman R L 2017 Comparison of shear velocity dispersion in viscoelastic phantoms measured by ultrasound-based shear wave elastography and magnetic resonance elastography *IEEE Int. Ultrasonics Symp.* (6–9 September 2017) pp 1–4
- Zhang W and Holm S 2016 Estimation of shear modulus in media with power law characteristics *Ultrasonics* **64** 170–6
- Zvietcovich F, Rolland J P, Meemon P and Parker K 2018 *Int. Tissue Elasticity Conf.* (Avignon, France)